



The effect of the elastic energy on the shape and orientation relations of η -Ni₃Ti precipitates in lath martensite



Mati Shmulevitsh^a, Sigalit Ifergane^a, Noam Eliaz^{b,*}, Roni Z. Shneck^{c,*}

^a Nuclear Research Center Negev, POB 9001, Beer Sheva 84190, Israel

^b Department of Materials Science and Engineering, Tel Aviv University, Ramat Aviv, Tel Aviv 6997801, Israel

^c Department of Materials Engineering, Ben-Gurion University of the Negev, POB 653, Beer Sheva 8410501, Israel

ARTICLE INFO

Article history:

Received 28 March 2022

Received in revised form 14 June 2022

Accepted 17 June 2022

Available online 20 June 2022

Keywords:

Elastic interaction energy

Lath martensite

Precipitation hardening

Custom 465° stainless steel

ABSTRACT

Understanding the elastic interaction between the precipitates may assist in controlling their distribution and help design new steels with enhanced mechanical properties. Custom 465° stainless steel contains only η -Ni₃Ti precipitates, making it an ideal steel to study the interaction and orientation relation (OR) between precipitates, which are known to grow in arrays parallel to the four closed-packed axes, $\langle 111 \rangle_{\text{bcc}}$, and closed-packed planes, $\{110\}_{\text{bcc}}$, of the matrix. This forms 144 possible orientation pairs, raising the question whether there are preferred relations between neighboring precipitates.

In this work we tackle this question by calculating the elastic fields and interaction between η -Ni₃Ti precipitates in bcc lath martensite in order to study the effect of elastic energy on the shape and orientation of the precipitates. The results of the calculations are compared to transmission electron microscopy (TEM) observations of Custom 465° stainless steel in different aging conditions. The calculations predict that the η -Ni₃Ti precipitates will favor an ellipsoidal morphology with a high aspect ratio. Experimentally, needle-shaped precipitates of $b/a = 3$ are observed in the steel in the peak-aged condition. Careful examination of the 144 possible orientation pairs reveals that they may be classified into five groups of crystallographically independent pairs of precipitates. The interaction energy of two precipitates reaches up to ~ 7% of the self-energy, higher than the typical interaction energy of precipitates in Ni-based superalloys. Here, the ORs between the precipitate is expected to occur in a more sophisticated manner along the four $\langle 111 \rangle$ branches. We provide evidence that effective interactions exist inside branches and between interpenetrating branches inclined at 109.5°, although they are not very clear since not all of the favored sites are occupied.

© 2022 Elsevier B.V. All rights reserved.

1. Introduction

Precipitation hardened steels are used in many applications, e.g. aircraft landing gear, rocket cases, high-performance shafts and tubes, and high-strength fasteners [1–4]. Moreover, understanding the relation between the precipitates may assist in controlling their distribution and help design advanced steels. In view of their wide applications, advanced structural steels are essential for sustainable future, reducing the environmental pollution in the steelmaking industry [1,2].

It has been realized that the body-centered cubic (bcc) ferritic/martensitic steels are ideal materials for strengthening by coherent nanoparticles [2]. Quenching low-carbon steel forms lath martensite

with a bcc structure, where a high density of precipitates grow during the aging process; this appears in steels such as traditional and advanced maraging steels (e.g., Custom 465°), ultrahigh-strength steels, etc. [3–13]. Among the precipitates that may nucleate during the aging process, hexagonal η -Ni₃Ti precipitates are common and effective strengthening phases [1]. Recently, a maraging steel that was characterized by atom probe tomography (APT) showed fast formation of η -Ni₃Ti precipitates at the beginning of the aging process, which could act as nucleation sites for latter precipitation of Ni₃Al and Ni₃Mo precipitates [9]. Ti additions have the highest strengthening effect by precipitating η -Ni₃Ti in some maraging steels [10,14]. Addition of Cu to Fe–Cr–Ni–Al–Ti maraging stainless steel provides nucleation sites for the precipitation of Ni₃(Ti,Al) by forming independent Cu clusters [15]. Furthermore, the synergistic effects among Mo, Ti, and Cr on nanoscale precipitation have been studied by APT and transmission electron microscopy (TEM) [16–18]. The APT results indicate that Mo partitions to the η -

* Corresponding authors.

E-mail addresses: [neliaz@tau.ac.il](mailto:neliz@tau.ac.il) (N. Eliaz), roni.shneck@gmail.com (R.Z. Shneck).

Ni_3Ti precipitate core in an early stage of precipitation, doubling the number density of Ni_3Ti precipitates. The formation of $\eta\text{-Ni}_3\text{Ti}$ precipitates consumes Ni from the matrix, which substantially inhibits the spinodal decomposition and refines the size of Cr-rich precipitates [16]. Plastic deformation of maraging steels also increases the density of $\text{Ni}_3(\text{Ti},\text{Mo})$ precipitates and promoted an earlier peak aging time and a higher peak hardness [19].

In most of the steels there are several types of precipitates, therefore their spatial distribution is complicated. Custom 465[®] (UNS S46500) is a martensitic age-hardenable stainless steel that contains only $\eta\text{-Ni}_3\text{Ti}$ precipitates, making it an ideal steel to study the interaction and orientation relations (ORs) between the precipitates. The $\eta\text{-Ni}_3\text{Ti}$ precipitate is known to have the shape of an elongated ellipsoid growing parallel to closed-packed directions and closed-packed planes of the matrix. Many observations [20–25] have shown arrays of precipitates parallel to the $\langle 111 \rangle_{\text{bcc}}$ directions, and recently the spatial distribution of $\eta\text{-Ni}_3\text{Ti}$ precipitates around the $\langle 111 \rangle_{\text{bcc}}$ in Custom 465[®] was measured by Rauch et al. [26]. Thus, the precipitates may form four intersecting arrays in space. TEM images appear to show random distribution of precipitates in each array. This calls for the following question which has not been answered before: Are there preferred relations between neighboring precipitates within an array and between intersecting arrays?

New particles formed in the initial stages of precipitation are coherent with the matrix. The coherent precipitates are associated with large elastic strains and energy. The tendency to reduce the elastic energy may influence the crystallographic structure, the shape and habit plane. For example, Ni_3Ti precipitates have fcc crystallographic structure and spherical shape in A-286 austenitic steel [27], or a cubic shape in Ni-based superalloys [28]. Changing the matrix to bcc structure leads to hcp crystallographic structure that favors needle-shaped precipitates [13]. Elastic interactions with other defects, e.g., other particles, dislocations and even twins, provide other avenues for saving energy, thereby influencing the alloy's properties [29–33]. Important interactions may set up among precipitates, giving rise to ORs between the precipitates; for example, Ni_3Ti precipitates in A-286 steel have weak interaction [27], while in Ni-based superalloys they exhibit almost a perfect ordering [28,34–37]. Precipitates in Al and Mg alloys also show high degree of ordering [33,38–41]. The elastic fields and interaction in a static lattice have been solved analytically by Eshelby, Khachaturyan, and Mura [54–56]. In the last decades, a new approach was applied to follow the development of microstructure in solids on large length and time scales [35,36,41]. These phase-field models define a mesoscopic free energy functional of the microstructure. At any time, the microstructure is represented by a set of continuous fields of the concentration and of long-range order parameters. The evolution of each field is obtained by solving a kinetic equation governed by its driving force. In this way, the evolution of the precipitate's size, shape and distribution are obtained. The phase-field approach has been applied to follow the development of precipitates in Ni-based superalloys with dilatational misfit [42,43], their coarsening and ordering [42–45], order formation due to elastic interactions among several variants with tetragonal misfit [45–47], selection of one variant out of several variants [44], spinodal [48] and martensitic [47] transformations. The effect of elastic inhomogeneity on these phenomena has been found by iterative solution of the field equations [27,42].

In this study, the elastic fields generated by coherent $\eta\text{-Ni}_3\text{Ti}$ precipitates in the bcc matrix are calculated, the interaction energy between precipitates is deduced, and hence its effect on their ORs is evaluated. The conclusions are compared to TEM observations of Custom 465[®] in different aging conditions.

2. Experimental

Custom 465[®] stainless steel was purchased from Carpenter Technology (Wyomissing, PA, USA). The chemical composition of the steel was determined by inductively coupled plasma atomic emission spectroscopy (ICP-AES) and inert gas fusion (IGF) analyses, yielding 10.9 Ni, 10.7 Cr, 1.4 Ti, 0.86 Mo, 0.04 Al, 0.04 Zn, and 0.0046 C (wt%), the remaining being Fe. The 2-inch diameter rod was received in the solution annealed (SA) and cold-treated condition, and was characterized in the SA and aged conditions in previous studies [13,49,50]. The steel was aged for four hours at several temperatures, corresponding to the definition of aging treatments of Custom 465[®]: $482 \pm 5 \text{ }^\circ\text{C}$ (H900), $510 \pm 5 \text{ }^\circ\text{C}$ (H950), $538 \pm 5 \text{ }^\circ\text{C}$ (H1000), $560 \pm 5 \text{ }^\circ\text{C}$ (H1040), $593 \pm 5 \text{ }^\circ\text{C}$ (H1100), $648 \pm 5 \text{ }^\circ\text{C}$ (H1200). Characterization of the precipitates in these aging conditions is provided elsewhere [13].

Samples in the SA and aged conditions were examined by JEOL JEM-2100 F TEM. TEM specimen preparation consisted of mechanical polishing to a 30- μm thickness on a 1000 grit SiC grinding paper, followed by mechanical polishing with 6 and 1 μm diamond pastes, using polishing cloths and water as lubricant. 3-mm diameter disks were cut using a punch, and the hole in the central area of the disk was ion-milled using a Gatan precision ion polishing system (PIPS) for electron transparency.

The ORs between the Ni_3Ti precipitates and the martensite matrix were $\{011\}_{\text{M}}//\{0001\}_{\text{Ni}_3\text{Ti}}$ and $\langle 111 \rangle_{\text{M}}//\langle 11\bar{2}0 \rangle_{\text{Ni}_3\text{Ti}}$, as calculated from Fig. 8a,b. As reported for Fe-20Ni-5Mn alloy [20,21,60], in the BF-TEM image (Fig. 4b) there are three variants of $\eta\text{-Ni}_3\text{Ti}$ precipitates at an angle of 60° from each other. A dark-field (DF) image taken at the $(22\bar{4}0)$ $\eta\text{-Ni}_3\text{Ti}$ reflection, which is parallel to the long axis of one of the variants of precipitates, revealed a rod-shaped morphology. For each aging treatment, the diameters and lengths of precipitates were examined and measured from DF images obtained at an identical crystallographic orientation: the $(22\bar{4}0)$ $\eta\text{-Ni}_3\text{Ti}$ reflection at $[112]_{\text{M}}$ zone axis of martensite.

3. Crystallographic analysis

In steels with lath martensite structure, TEM observations reveal rod-shaped $\eta\text{-Ni}_3\text{Ti}$ precipitates with their long axis being parallel to the $\langle 111 \rangle$ directions in the matrix phase. The ORs between the hexagonal precipitates ($a = 0.5101 \text{ nm}$, $c = 0.8307 \text{ nm}$) [51] and the bcc lath martensite ($a = 2.878 \text{ nm}$) [52] are: $\langle 111 \rangle_{\text{M}}//\langle 11\bar{2}0 \rangle_{\text{Ni}_3\text{Ti}}$, $\{011\}_{\text{M}}//\{0001\}_{\text{Ni}_3\text{Ti}}$.

There are several possible orientations to situate the dense planes and directions in the hexagonal second phase to lay parallel to the dense planes and directions in the bcc matrix, e.g. according to Pitsch-Schrader (P-S) or Burgers [53]. Fig. 1 shows hexagonal group of atoms in the precipitate (red hexagon) and in three bcc unit cells of the matrix (blue hexagon). Fig. 1a illustrates the P-S ORs in which the $\langle 100 \rangle_{\text{bcc}}$ and $\langle 1\bar{1}0 \rangle_{\text{bcc}}$ directions are parallel to the $\langle 2110 \rangle_{\text{hcp}}$ and $\langle 01\bar{1}0 \rangle_{\text{hcp}}$ directions, respectively. In order to generate the Burgers relation between the hexagonal basal plane of $\eta\text{-Ni}_3\text{Ti}$ and the irregular hexagonal (110) plane of the bcc matrix [21,25,26,53], the $[2110]$ directions in the $\eta\text{-Ni}_3\text{Ti}$ have to be rotated by 5.26° relative to the nearest $\langle 111 \rangle$ direction of the matrix, as shown in Fig. 1b. It turns out that if Burgers is associated with smaller mismatch both quantitatively and experimentally, this is the observed relation [21,25,26]. Fig. 8a,b shows selected area electron diffraction (SAED) micrographs supporting the actual ORs between the precipitates and the matrix.

The misfit strain calculated in the coordinate axes $x = [\bar{1}11]$, $y = [\bar{1}1\bar{2}]$, $z = [110]$ is:

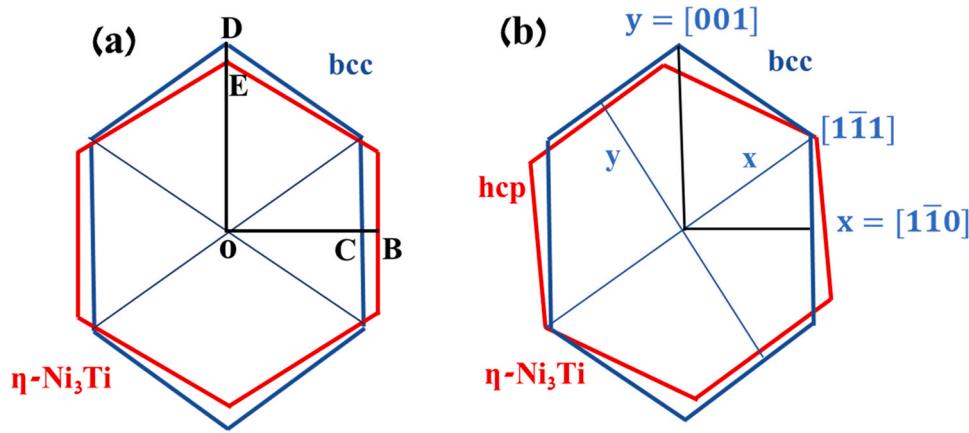


Fig. 1. (a) Illustration of the P-S orientation relation between the hcp precipitate $\eta\text{-Ni}_3\text{Ti}$ and the bcc martensite matrix before being rotated by 5.26° . (b) The Burgers orientation in the xy plane between the bcc matrix and $\eta\text{-Ni}_3\text{Ti}$ (after being rotated by 5.26°) causes shear, extension and contraction in two perpendicular directions (see Fig. 4).

$$\tilde{\varepsilon}_{xyz} = \begin{pmatrix} 0.02257 & -0.0904 & 0 \\ -0.0904 & -0.0606 & 0 \\ 0 & 0 & 0.0198 \end{pmatrix} \quad (1)$$

The misfit strain in the bcc coordinate system ($x' = [110]$, $y' = [010]$, $z' = [001]$) is found by the transformation equation of a second-rank tensor, $\varepsilon'_{ij} = a_{ik}a_{jl}\varepsilon_{kl}$

$$\tilde{\varepsilon}_{x'y'z'}^T = \begin{pmatrix} 0.0499 & -0.0301 & -0.0064 \\ -0.0301 & 0.0499 & 0.0064 \\ -0.0064 & 0.0064 & -0.1181 \end{pmatrix} \quad (2)$$

4. Calculation method

The displacements u_i^0 due to the homogeneous precipitate in Eq. (3) have been expressed as a Fourier series in [54,55]:

$$u_i^0(\mathbf{x}) = \sum_{\mathbf{k}} (C_{klmn}\varepsilon_{mn}^T\theta_{ik}\Omega_{ik})\exp(i\mathbf{k}\cdot\mathbf{x}) \quad (3)$$

where summation should be taken over the reciprocal space vectors \mathbf{k} , Ω is the Fourier transform of the Green function defined by $\Omega_{ij}^{-1}(\mathbf{k})$, $C_{ijmn}k_mk_n$ and C_{klmn} are the elastic constants, ε_{mn}^T are the transformation strains as defined in Eq. (2), and $\theta(r)$ is the shape function of the precipitate, defined as unity in the precipitate and zero in the matrix. We approximate the shape of the precipitate by an ellipsoid with an aspect ratio of 1:3 (Fig. 2). For the case of multi-particle system, the shape function of particles displaced from the origin, $\theta(\mathbf{k})$, is conveniently calculated from the shape function of particles centered in the origin of coordinated $\theta_0(\mathbf{k})$ by applying the Fourier displacement theorem:

$$\theta(\mathbf{k}, \mathbf{d}) = \theta_0(\mathbf{k}) \exp(-i\mathbf{k}\cdot\mathbf{d}) \quad (4)$$

The elastic strains are derived from the compatibility equation, and the stresses are related to the strains by Hooke's law.

In order to calculate the total elastic energy in the system one has to integrate the products of elastic stresses and strains over the volume of the whole system, including the precipitates and matrix:

$$E_{self} = \frac{1}{2} \int_{\infty} \sigma_{ij}\varepsilon_{ij} dV = \frac{1}{2} \int_{V_p} \sigma_{ij}\varepsilon_{ij}^T dV \quad (5)$$

Esheby [56] proved that the total elastic energy can be expressed as an integral only over the volume of the precipitate alone, as expressed by the last term in Eq. (5). He also proved that the interaction energy between two precipitates can be calculated as an integral of the stresses produced by one precipitate A over the volume of the neighboring particle B:

$$E_{int} = -\frac{1}{2} \int_{VB} \sigma_{ij}^A \varepsilon_{ij}^{T,B} dV = -\frac{1}{2} \int_{\infty} \sigma_{ij}^A \varepsilon_{ij}^{T,B} \theta(r) dV \quad (6)$$

According to Parseval's theorem, the integral over the whole space of a product of functions in the real space is equal to the integral on their Fourier transforms over the whole reciprocal space

$$E_{int}(\mathbf{d}) = -\frac{1}{2} \int_{\infty} \sigma_{ij}^A(\mathbf{r}) \varepsilon_{ij}^{T,B} \theta(\mathbf{r}) d^3r = -\frac{1}{2} \int_{\infty} \sigma_{ij}^A(\mathbf{k}) \varepsilon_{ij}^{T,B} \theta_0(\mathbf{k}) \exp(-i\mathbf{k}\cdot\mathbf{d}) d^3k \quad (7)$$

This equation, first written by Khachauryan [55], makes it possible to obtain the interaction energy of particle A with particles B located at any point \mathbf{d} in the space around particle A by a single application of the Fast Fourier Transform (FFT) algorithm. All the sums in the present work were calculated employing this algorithm with 256^3 terms. The elastic constants representing the bcc matrix were taken as the constants of pure α -iron [57]: $C_{11} = 232$ GPa, $C_{12} = 136$ GPa, $C_{44} = 117$ GPa.

In order to apply the analytic solution for several precipitates one has to assume homogenous system, namely that the elastic constants of the precipitates and the matrix are equal. Ordinarily, there is a small variation in the elastic constants among metals, and estimations of the variation in energy due to the assumption of homogeneity show that it introduces only small differences [58,59]. The homogeneity assumption also allows the use of linear superposition of several precipitates [56].

5. Results and discussion

5.1. The preferred shape and the self-energy

Fig. 2a describes the calculated elastic energy in $\eta\text{-Ni}_3\text{Ti}$ precipitates in the matrix as a function of the shape of the precipitate. The assumed shapes are ellipsoids of revolution with $a = c \neq b$; thus, the shape of the precipitate varies from a disk shape, through a sphere ($b/a = 1$) to a needle shape as the aspect ratio b/a increases (the black curve). The results predict that the $\eta\text{-Ni}_3\text{Ti}$ precipitates will favor an ellipsoid-shaped morphology with a high aspect ratio. Experimentally, needle-shaped precipitates with about $b/a = 3$ (Fig. 2b), are observed in Custom 465[®] in the peak-aged conditions (H900 and H950); they are characterized by maximal values of hardness [13]. As the precipitates lose their coherency due to overaging (Fig. 2c), their aspect ratio increases up to $b/a \sim 5$ at a temperature of 648°C (H1200). At this stage, the effect of the elastic energy reduces, and the contribution of the surface energy is minor,

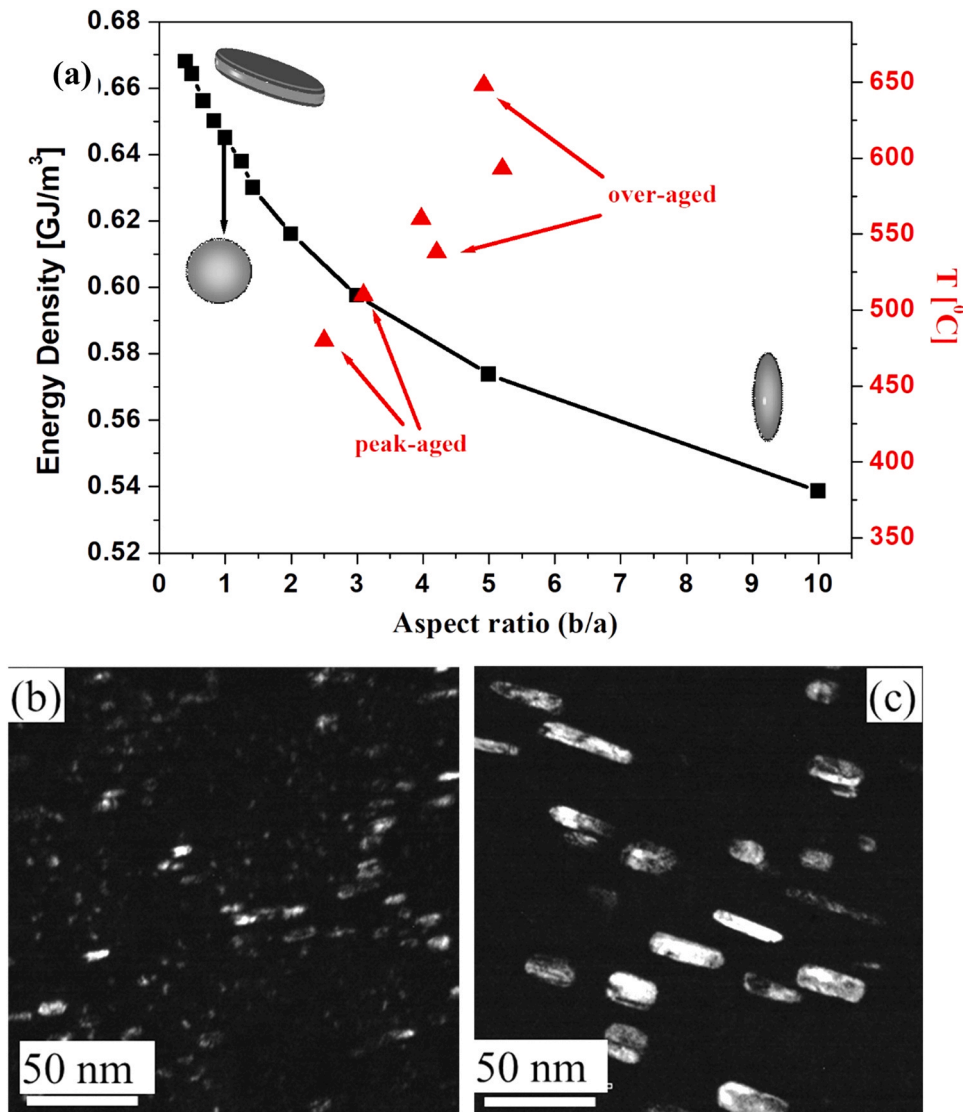


Fig. 2. (a) The elastic energy of the system of a η -Ni₃Ti precipitate and a matrix per unit volume of the precipitate as a function of its shape. The red dots represent the aspect ratios of experimentally observed precipitates at different aging temperatures. TEM DF images from the (2240) reflection of one variant of the η -Ni₃Ti precipitates in Custom 465° stainless steel after aging in the peak-aged H950 (b) and overaged H1040 (c) conditions.

therefore one may assume that anisotropic interface mobility is responsible for the elongated shape.

Fig. 3 describes strain maps of the resulting equilibrium between a η -Ni₃Ti precipitate and the bcc matrix. Fig. 3a presents the ϵ_{xx} in the X-Y plane, while Fig. 3b,c describes the ϵ_{yy} and ϵ_{zz} strains, respectively, in the dense (1 $\bar{1}$ 0) plane. The effects of the strains are of short range and give rise to compressive radial stresses and to tensile tangential stresses in the matrix.

5.2. The elastic interaction between η -Ni₃Ti precipitates

TEM observations show that precipitates grow such that their close-packed planes and directions are parallel to the close-packed planes and directions in the matrix. There are four equivalent $\langle 111 \rangle$ directions in the bcc lattice (Fig. 4a). The angle between each pair of $\langle 111 \rangle$ directions is 109.5° (or 70.5°). Fig. 4b is a bright-field (BF) TEM image of η -Ni₃Ti precipitates, demonstrating three out of four different orientations after H1000 aging treatment.

The crystallographic orientation of a precipitate parallel to a certain $\langle 111 \rangle$ direction is, however, not unique since the close-packed plane may lie parallel to one out of three {110}_{bcc} planes of

the matrix that contain the same $\langle 111 \rangle$ axis. In each variant, one principal strain is parallel to the $\langle 111 \rangle$ axis, the second is normal to the same axis in the same plane, and the third is normal to the habit plane. The principal strains are common in all variants; they differ only by the orientation of these strains. Fig. 4c illustrates three possible habit planes available for a precipitate laying parallel to the [111] axis and the three possible habit planes available for a second precipitate laying parallel to the [11 $\bar{1}$] axis, along with the transformation strains (in the x,y,z axes) associated with each orientation.

Therefore, there are 12 crystallographic variants of single precipitates, and 144 possible orientation variants of pairs of precipitates (see Appendix). Careful examination of these variants reveal that they may be classified into five groups of crystallographically independent pairs of precipitates, illustrated in Figs. 5–7. Table 1 describes each crystallographic group and the maximum value of the elastic interaction between each pair. The highest interaction energy is obtained for pairs of parallel, co-axial precipitates with habit planes intersected at 60°. Lower values are obtained for parallel pairs of co-axial precipitates laying on the same habit plane, or pairs of precipitates laying along intersecting axes with habit planes intersecting at 60°. The remaining orientations

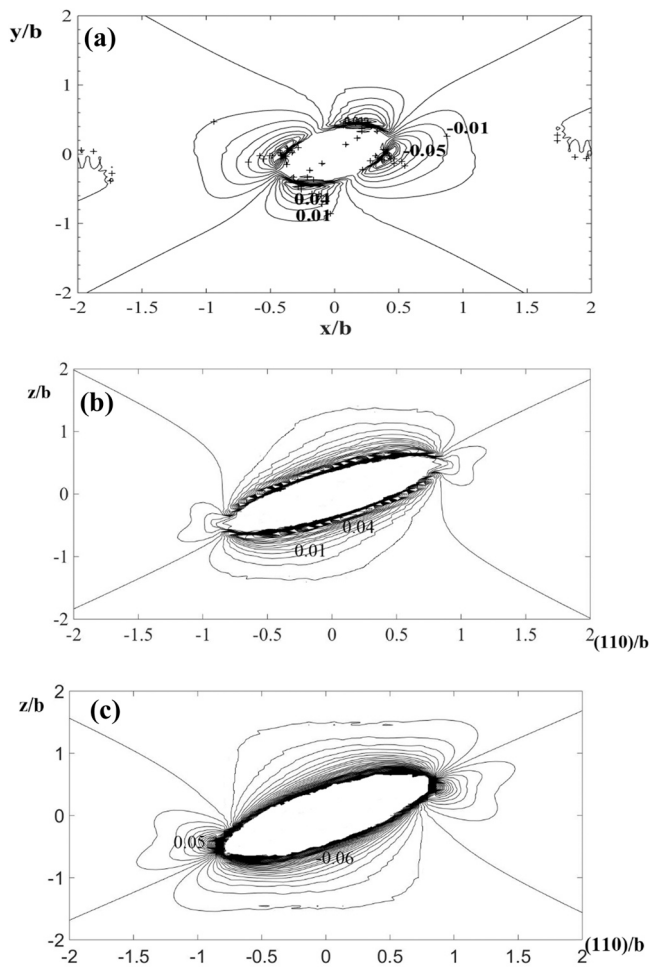


Fig. 3. Selected maps of the strains generated by a η -Ni₃Ti precipitate in equilibrium with the bcc matrix: (a) the ϵ_{xx} in the X-Y plane, (b) the ϵ_{yy} in the dense (110) plane, (c) the ϵ_{zz} in the dense (110) plane.

have interaction energy three times smaller than the maximal interaction.

The self-energy of two η -Ni₃Ti precipitates is about 1.2 GJ/m³ and the interaction energy of parallel precipitates reaches ~ 7% of the self-energy in OR (a), and ~ 5% of the self-energy in ORs (b) and (c). The typical order of magnitude of interaction energy that gives rise to exemplary ORs of precipitates in Ni-based superalloys along the three $\langle 100 \rangle$ axes is about 5% of the self-energy that is lower by an order of magnitude than self-energy in Custom 465° [34,35]. Here, the ORs are expected to occur in a more sophisticated manner along the four $\langle 111 \rangle$ axes (Fig. 4a), and this is probably the reason that these ORs between the precipitates have not been described in earlier studies.

In Figs. 5–7, representative maps of the interaction energies in the three combinations with highest interaction energies are shown. Each map describes the interaction between a precipitate located at $[-0.7, 0, 0]$ length units behind the center of the map, and a second precipitate surrounds it (see calculation method in Section 4). Three types of sites are found: (a) energy minima, where attractive interactions are obtained when stresses generated by one precipitate overlap with stresses with the opposite sign generated by a neighboring precipitate; (b) energy maxima, where the repulsive interactions are obtained when stresses generated by one precipitate overlap with stresses with the same sign generated by a neighboring precipitate; (c) between the energy extrema are regions of relative indifference.

Figs. 5a and 6a illustrate the interaction energy maps in the (110) plane between two parallel η -Ni₃Ti precipitates with equal size, exhibiting the highest interaction. The first case represents precipitates laying on habit planes inclined at 60°, whereas the second case is associated with two parallel precipitates with the same habit planes (see Table 1, ORs (a) and (b)). In both cases, the highest interaction is found when the precipitates are in proximity, displaced by approximately two radii between each other. The centers of interacting precipitates are slightly diverted from each other, located side-by-side in OR (a) or head-to-tail in OR (b). Figs. 5b and 6b show maps of the ϵ_{xx} strain in the (110) plane of two parallel η -Ni₃Ti precipitates located in the respective highest interaction configurations. Both figures illustrate the overlap between strains set up in the matrix due to the misfitting precipitates. The strains in Fig. 5b are different in the two precipitates since their habit planes are different, while the strains in Fig. 6b are similar since the habit planes are parallel. Fig. 5c,d are real BF and DF TEM images of needle-shaped η -Ni₃Ti precipitates with side-by-side or head-to-tail relations at almost touching proximity of parallel precipitates that is very similar to the configurations predicted by the maps of interaction energy. The DF image in Fig. 5d reveals that some of the precipitates vanished since they are laying parallel to a different habit plane while others sustain since the co-axial precipitates lay on parallel habit planes.

Fig. 7a presents the interaction energy map on the (110) plane of two precipitates inclined at 109.5° (or 70.5°) to each other since their long axes are parallel to different $\langle 111 \rangle$ axes and habit planes intersecting by 60° (OR (c)). Fig. 7b describes the map of the ϵ_{xx} strain on the (110) plane of two parallel η -Ni₃Ti precipitates with 1:3 aspect ratio positioned at the highest interaction configuration. As in the case of precipitates that are parallel to each other, the favored relation is observed when the precipitates are almost in touching each other. Fig. 7c,d shows TEM images of η -Ni₃Ti precipitates. The images conform with the orientation of 109.5° between the precipitates that was expected from their relation to the $\langle 111 \rangle$ axes. Notably, precipitates with touching proximity are commonly observed, in line with the calculations presented as energy maps (Fig. 7a). Moreover, The DF image in Fig. 7d demonstrate that only one of the needle-shaped η -Ni₃Ti precipitates can be seen, implying that the precipitates are laying in different habit planes conforming with OR (c) and OR (e). Since the multiplicity and the interaction energy of OR(c) is significantly higher than those of OR (e), it is most probable that the image represents OR(c).

It is possible that the precipitates that appear adjacent to each other in TEM images lie far below each other in the real space. Indeed, it is expected that the precipitates laying on different $\langle 111 \rangle$ axes will be inclined at 109°, but their frequent proximity indicates that this is an outcome of interaction between the precipitates. The same alloy was carefully studied by TEM by Rauch and Veron [26]. In their study, many proximate pairs of parallel and 109°-inclined precipitates were observed. Direct support of our assumptions was provided by APT studies [15,17,19] of η -Ni₃Ti precipitates in lath martensite maraging steels, exhibiting relatively large abundance of the said ORs.

How these tendencies combine in the real three-dimensional (3D) arrangement of many precipitates is difficult to grasp. The arrangement along the dense $\langle 111 \rangle$ orientations and {110} planes is evident in the TEM observations (Fig. 8). TEM DF images illustrate clusters of parallel precipitates along the different $\langle 111 \rangle$ orientations (Fig. 8c,d). This is clear since the self-elastic energy of each precipitate is determined by the best fitting of closed-packed orientations (Fig. 8a,b). The interaction between different branches is not obvious experimentally in Custom 465° stainless steel, as demonstrated by the TEM BF images in Fig. 8e,f, due to four reasons: (a) the low volume fraction (6 vol%) of precipitates hinders the occupation of all the favored sites; (b) the interaction energies are

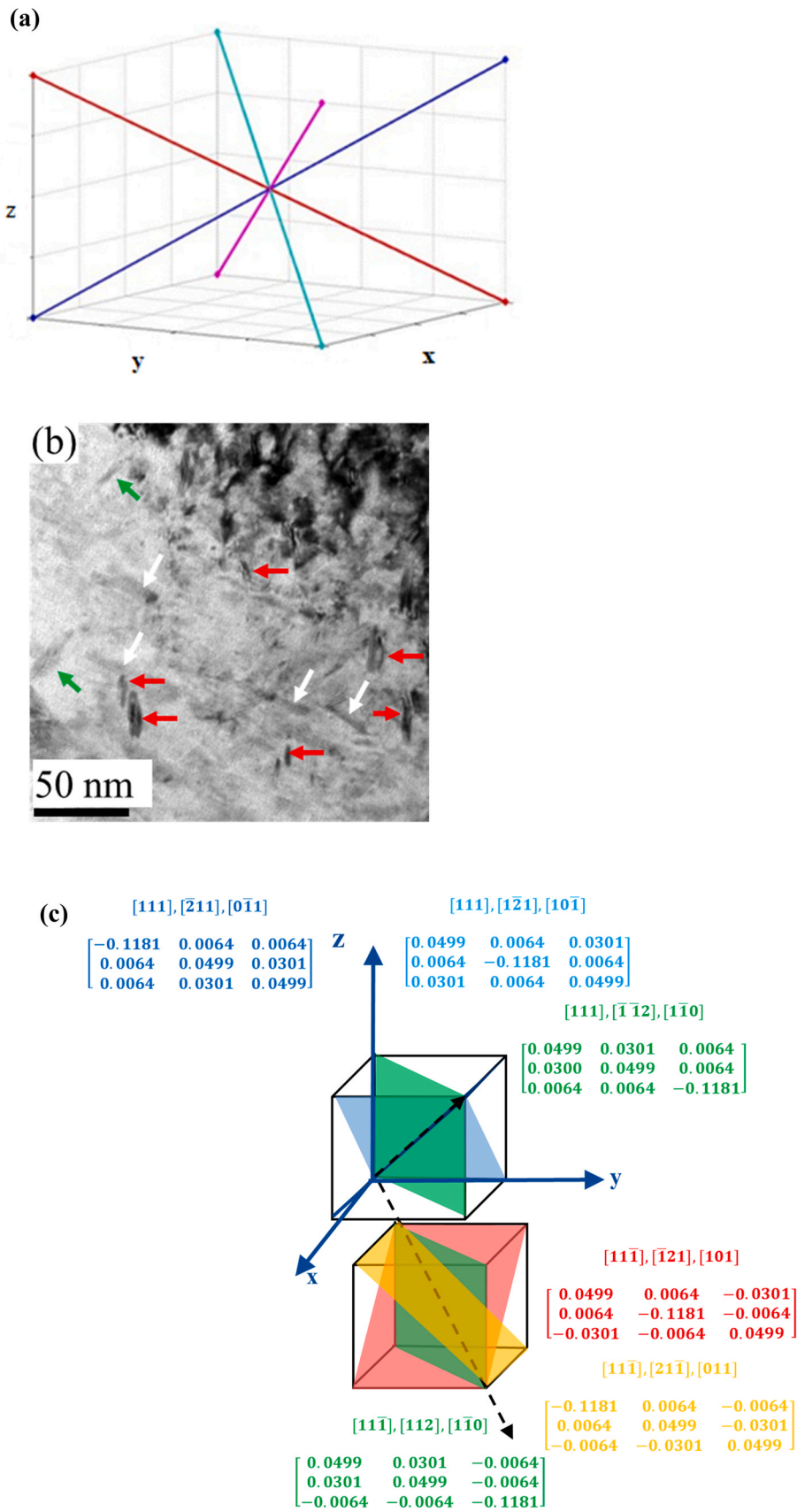


Fig. 4. (a) The four $\langle 111 \rangle$ directions in space. (b) TEM BF taken at zone axis $[112]_M$, image of η - Ni_3Ti precipitates along three different axes in the H1000 condition. (c) Two representatives $\langle 111 \rangle$ axes and the three possible habit planes along each axis, along with the transformation strains, in the xyz coordinate system, associated with each orientation. These strains are obtained by the proper transformations of Eq. (2).

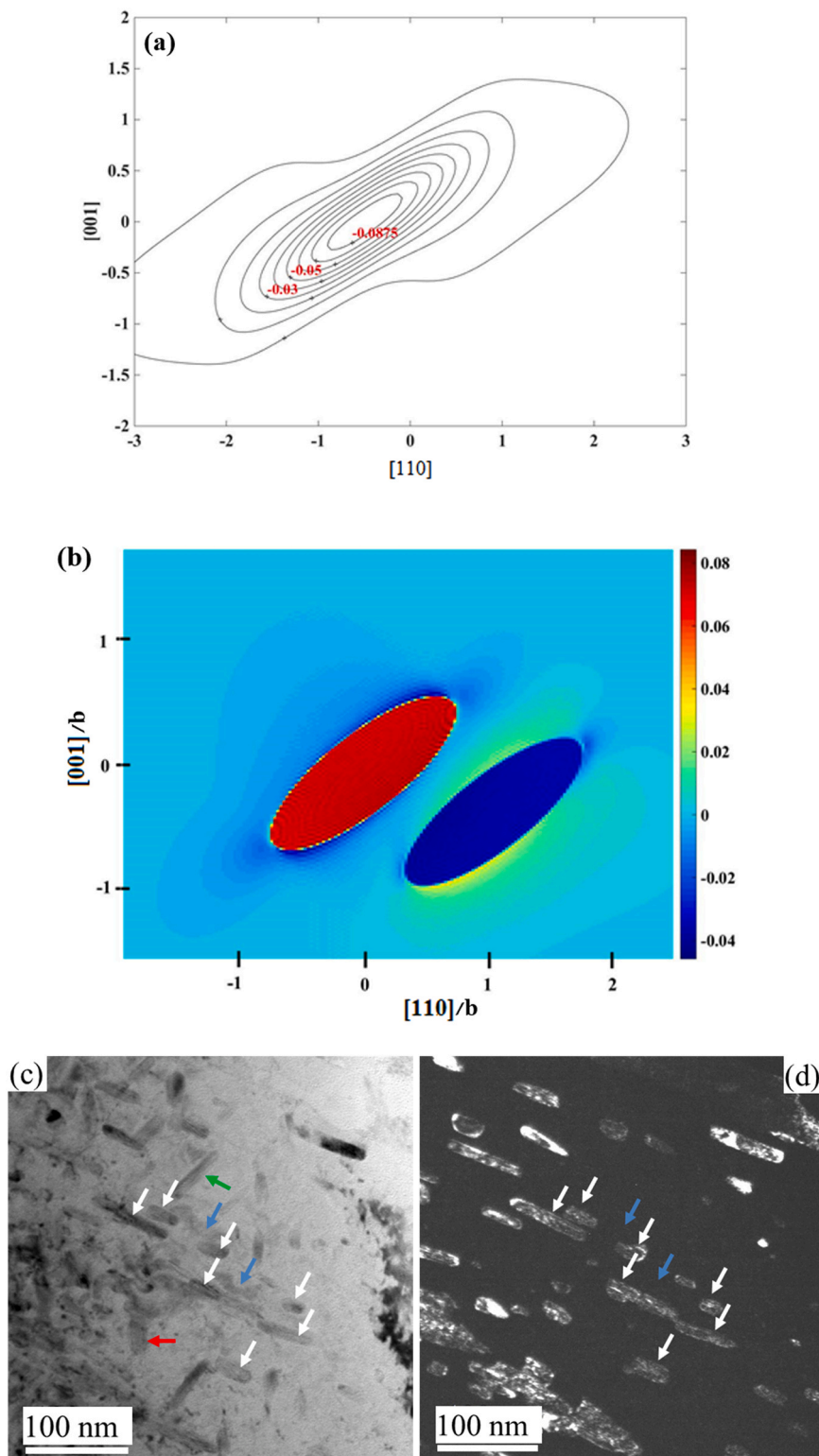


Fig. 5. (a) The interaction energy map on the (110) plane between two parallel η - Ni_3Ti precipitates with equal size laying on habit planes inclined at 60° . (b) A map of the ϵ_{xx} strain generated by the two precipitates positioned in the highest interaction configuration in (a). (c) TEM BF image taken at zone axis $[112]_M$ of η - Ni_3Ti precipitates in the H1100 condition. The white and the blue arrows point at parallel precipitates. (d) DF image from the (2240) reflection of one variant of the η - Ni_3Ti precipitates. Marked by blue arrows are precipitates that vanish since they are laying parallel to different habit planes, while precipitates with parallel habit planes remain visible and marked by white arrows. Adapted from Fig. 3 in Ref. [13], with permission from Elsevier.

Table 1 F

Five groups of crystallographically independent pairs of precipitates classified by the orientation relation (OR), the number of pairs in each OR, and the elastic interaction between them per unit volume of the precipitates.

	Orientation Relation (OR)	No. of pairs	E_{int} (MJ/m ³)
(a)	Co-axial precipitates with habit planes intersecting at 60°	24	-87.5
(b)	Co-axial precipitates with parallel habit planes	12	-60
(c)	Precipitates laying along intersecting axes, with habit planes intersecting at 60°	72	-62
(d)	Precipitates laying along intersecting axes, with parallel habit planes	12	-33
(e)	Precipitates laying along intersecting axes, with habit planes intersecting at 90°	24	-28

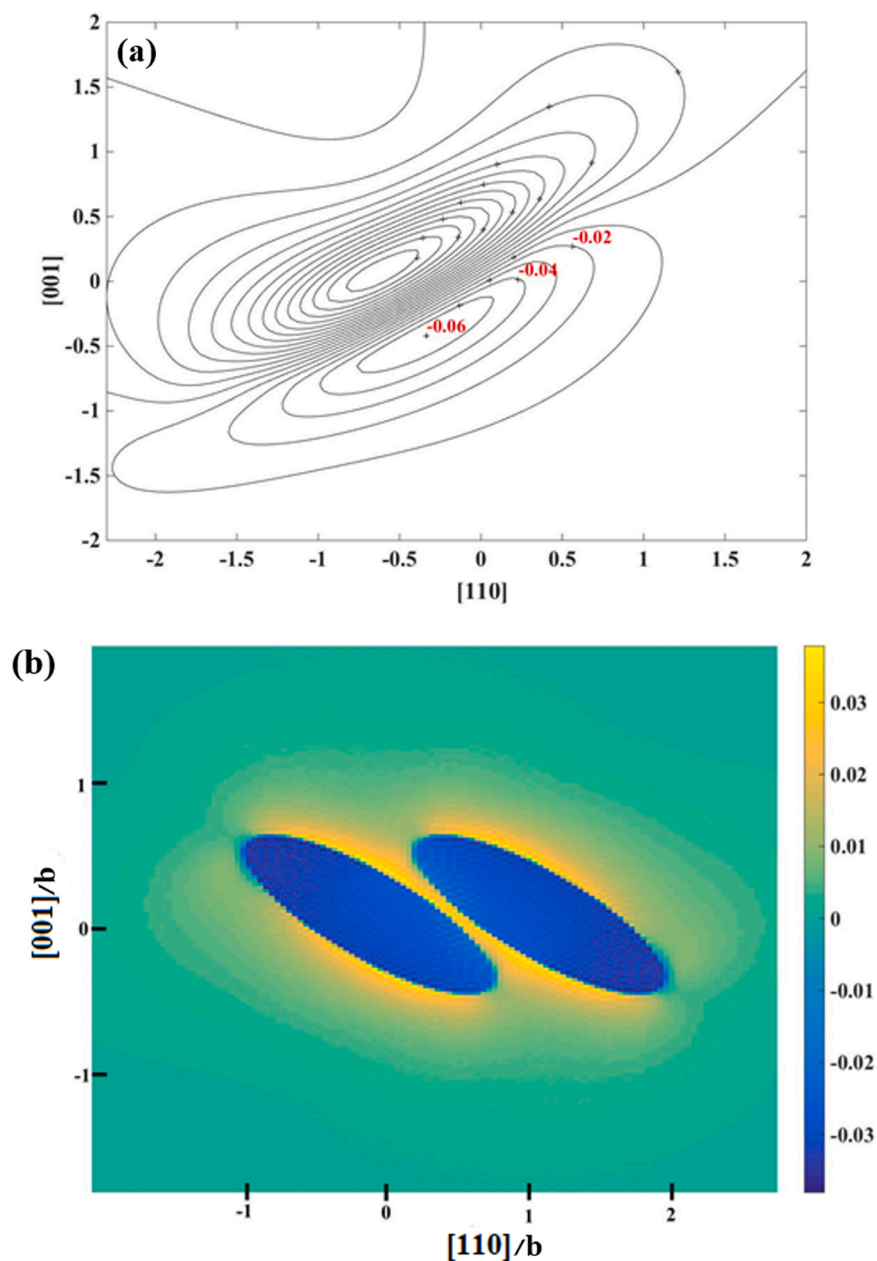


Fig. 6. (a) The interaction energy maps on the (110) plane between two parallel η -Ni₃Ti precipitates with the same habit planes. (b) Map of the ϵ_{xx} strain in the (110) plane of two parallel η -Ni₃Ti precipitates located at the highest interaction configuration.

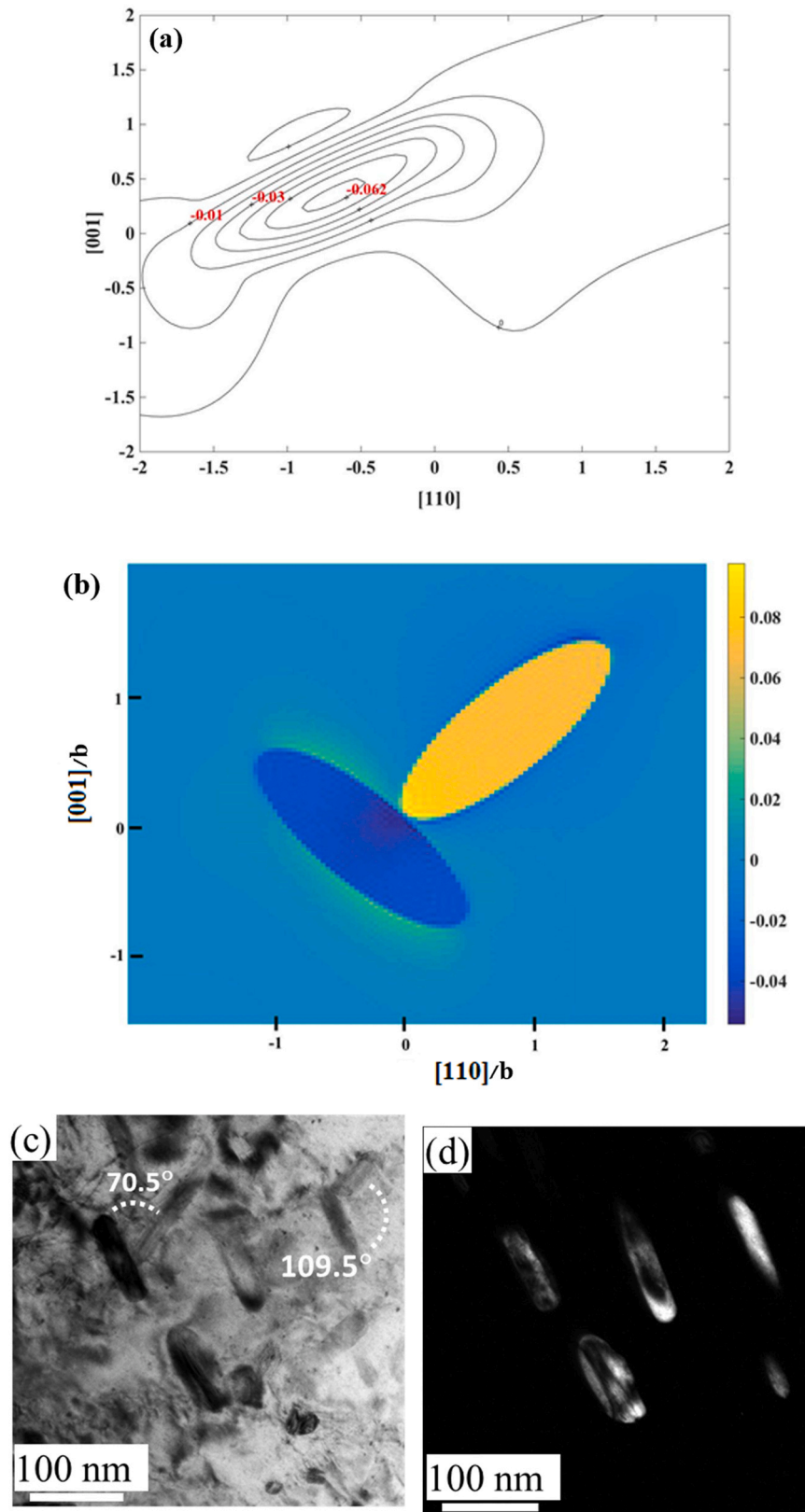


Fig. 7. (a) Interaction energy map on the (110) plane of two precipitates inclined at 109.5° (or 70.5°) to each other and habit planes intersecting by 60° . (b) A map of the ϵ_{xx} strain generated by the two precipitates positioned in the highest interaction configuration in (a). (c) TEM BF image taken at zone axis $[112]_M$ of η - Ni_3Ti precipitates in the H1150 aging condition, showing two precipitates inclined at 109.5° and another pair inclined at 70.5° . (d) DF image from the (2240) reflection of one variant of the η - Ni_3Ti precipitates. The figure reveals that some of the precipitates vanish since they are laying in different habit planes. Adapted from Fig. 3 in Ref. [13], with permission from Elsevier.

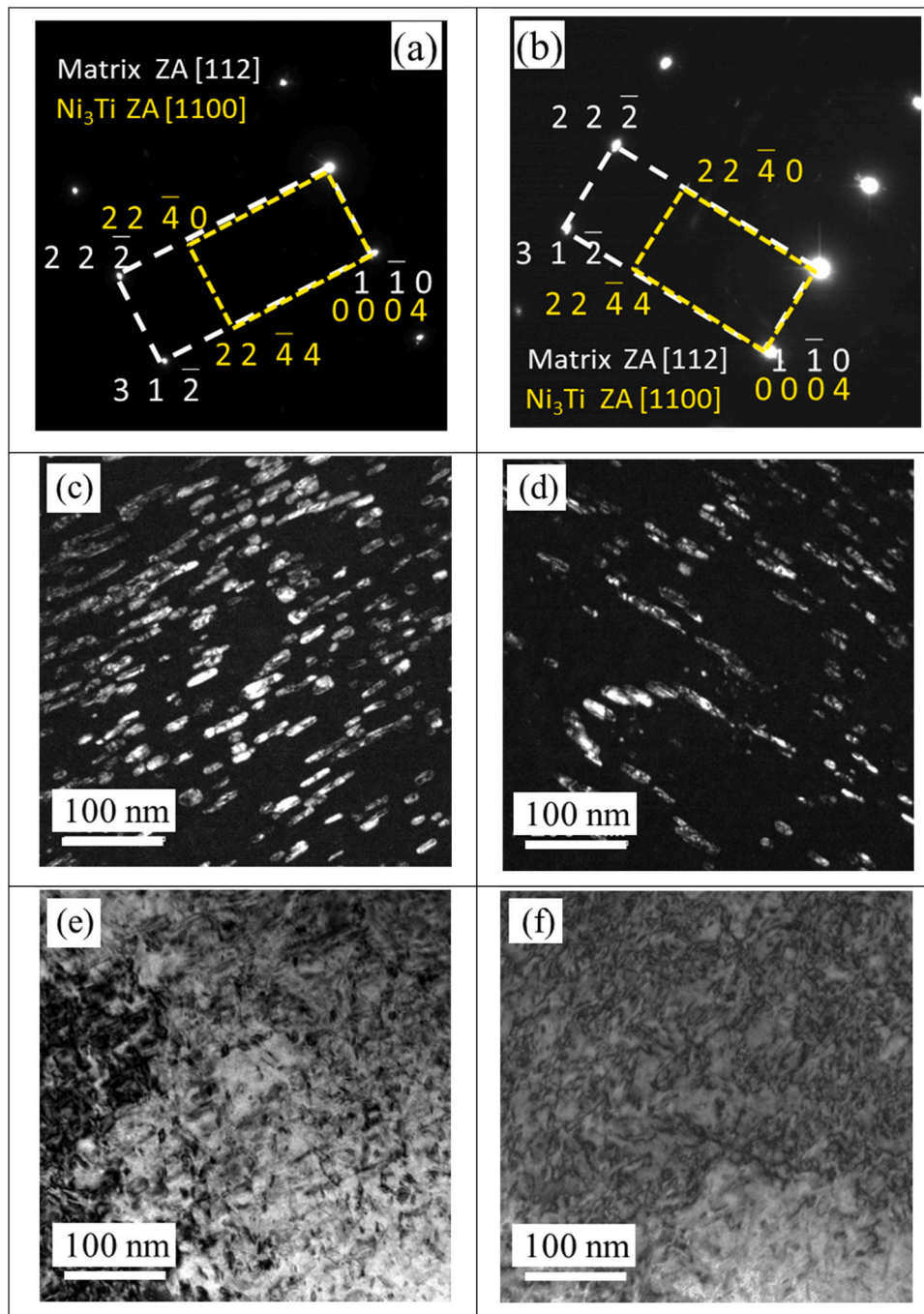


Fig. 8. Custom 465° stainless steel in the H1000 aging condition, observed in two orientations inclined at 120°. (a,b) SAED micrographs describing the orientation relations between precipitates and the matrix. (c, d) TEM DF images associated with the (2240) reflection of two variants of the η -Ni₃Ti precipitate, revealing dense precipitate clouds surrounded by less populated regions. (e, f) TEM BF images at the two orientations.

much lower than the self-elastic energy; (c) the observation conditions in the TEM hinders the simultaneous observation of all the existing orientations; (d) the precipitates are arranged along four axes in a 3D space. The interaction energy in the Custom 465° steel is larger than that in Ni-based superalloys in absolute magnitude, yet ordering in the steel is not obvious as in superalloys. The main reason for the lack of clear ordering is most likely the low volume fraction of precipitates. Experimentally, the precipitates often appear in dense clouds surrounded by less populated regions (Fig. 8c,d). These clouds may indicate preferred nucleation around some primary precipitates. In this study, evidence is provided that

effective interactions exist inside branches and between interpenetrating branches, as observed in Figs. 5c,d and 7c,d.

6. Conclusions

The effect of the elastic energy on the shape and orientation relations (ORs) between η -Ni₃Ti precipitates in lath martensite was studied using the quasi-analytic Fourier transform method and TEM observations of Custom 465° stainless steel. Since the precipitates are growing in arrays parallel to the four closed-packed axes, $\langle 111 \rangle_{\text{bcc}}$, and closed-packed planes, $\{110\}_{\text{bcc}}$, of the matrix, there are 144

possible orientation-pairs, which are classified herein into five groups of crystallographically independent pairs. Accordingly, the elastic interaction energy within each group was calculated. The following conclusions were drawn:

1. The η -Ni₃Ti precipitates favor an ellipsoidal shape with a high aspect ratio. Experimentally, needle-shaped precipitates with ca. $b/a=3$ are observed in Custom 465® in the peak-aged condition.
2. The interaction energy of two precipitates reaches up to ~ 7% of the self-energy, higher than the typical interaction energy of precipitates in Ni-based superalloys. In steels, the ORs between the precipitates are expected to occur in a more sophisticated manner along the four $\langle 111 \rangle$ axes.
3. The top three orientation relations that represent the highest interactions are when the precipitates are parallel to each other or when they are laying along intersecting axes with habit planes intersecting at 60°. In those orientation relations, the highest interaction is found when two precipitates touch each other and are positioned either side-by-side or head-to-tail. These predictions are in good agreement with TEM observations of individual pairs.
4. The precipitates often appear in dense clouds surrounded by less populated regions. These clouds may indicate preferred nucleation around some primary precipitates that interact with the

others. However, the low volume fraction of precipitates (6 vol%) in Custom 465® hinders the occupation of all of the favored sites, and the observation conditions in the TEM makes it difficult to observe simultaneously all of the existing orientations. It is noteworthy that uneven density of precipitates gives rise to non-homogeneous mechanical properties on the microscopic scale.

CRediT authorship contribution statement

M. Shmulevitch: Conceptualization, Data curation, Investigation, Validation, Visualization, Writing – original draft. **S. Ifergane:** Data curation, Investigation, Visualization, Writing – review & editing. **N. Eliaz:** Funding acquisition, Supervision, Visualization, Writing – review & editing. **R. Shneck:** Conceptualization, Supervision, Writing – original draft.

Declaration of Competing Interest

The authors declare that they have no known competing financial interests or personal relationships that could have appeared to influence the work reported in this paper.

Appendix

The 144 combinations of crystallographically independent pairs of precipitates, classified according to the orientation relations (ORs) between the dense axes and the dense planes in the bcc matrix. 1: co-axial precipitates with parallel habit planes, 2: co-axial precipitates with habit planes intersecting by 60°, 3: precipitates lying along intersecting axes with parallel habit planes, 4: precipitates lying along intersecting axes with habit planes intersecting by 60°, 5: precipitates lying along intersecting axes with habit planes intersecting by 90°.

	$[11\bar{1}]$, (110)	$(1\bar{1}0)$	$[11\bar{1}]$, (011)	$[1\bar{1}\bar{1}]$, (110)	$[1\bar{1}\bar{1}]$, (011)	$[1\bar{1}\bar{1}]$, (011)	$(10\bar{1})$	$[1\bar{1}\bar{1}]$, (110)	$[1\bar{1}\bar{1}]$, (101)	$[11\bar{1}]$, (011)	$[111]$, (011)	$(1\bar{1}0)$	$[111]$, (011)	$[111]$, (101)
$[11\bar{1}]$, $(1\bar{1}0)$	1	2	2	5	4	4	5	4	4	3	4	4	4	4
$[11\bar{1}]$, (101)	2	1	2	4	4	5	4	3	4	4	4	4	5	5
$[11\bar{1}]$, (011)	2	2	1	4	3	4	4	4	5	4	5	4	4	4
$[1\bar{1}\bar{1}]$, (110)	5	4	4	1	2	2	3	4	4	5	4	4	4	4
$[1\bar{1}\bar{1}]$, (011)	4	4	5	2	1	2	4	4	5	4	5	4	4	4
$[1\bar{1}\bar{1}]$, $(10\bar{1})$	4	3	4	2	2	1	4	5	4	4	4	4	4	3
$[1\bar{1}\bar{1}]$, (110)	5	4	4	3	4	4	1	2	2	5	4	4	4	4
$[1\bar{1}\bar{1}]$, (-101)	4	3	4	4	4	5	2	1	2	4	4	4	5	5
$[1\bar{1}\bar{1}]$, (-011)	4	4	5	4	5	4	2	2	1	4	3	4	4	4
$[111]$, $(1\bar{1}0)$	3	4	4	5	4	4	5	4	4	1	2	2	2	2
$[111]$, $(0\bar{1}1)$	4	4	5	4	5	4	4	4	5	2	1	2	2	2
$[111]$, $(10\bar{1})$	4	5	4	4	4	3	4	3	4	2	2	2	1	1

References

- [1] J.W. Morris, Making steel strong and cheap, *Nat. Mater.* 16 (2017) 787–789, <https://doi.org/10.1038/nmat4949>
- [2] Z.B. Jiao, J.H. Luan, M.K. Miller, Y.W. Chung, C.T. Liu, Co-precipitation of nanoscale particles in steels with ultra-high strength for a new era, *Mater. Today* 20 (2017) 142–154, <https://doi.org/10.1016/j.mattod.2016.07.002>
- [3] W. Xu, P.E.J. Rivera-Díaz-del-Castillo, W. Wang, K. Yang, V. Bliznuk, L.A.I. Kestens, S. van der Zwaag, Genetic design and characterization of novel ultra-high-strength stainless steels strengthened by Ni₃Ti intermetallic nanoprecipitates, *Acta Mater.* 58 (2010) 3582–3593, <https://doi.org/10.1016/j.actamat.2010.02.028>
- [4] C. Shen, C. Wang, X. Wei, Y. Li, S. van der Zwaag, W. Xu, Physical metallurgy-guided machine learning and artificial intelligent design of ultrahigh-strength stainless steel, *Acta Mater.* 179 (2019) 201–214, <https://doi.org/10.1016/j.actamat.2019.08.033>
- [5] R.F. Decker, J.T. Eash, A.J. Goldman, Eighteen percent nickel maraging steel, *Trans ASM* 55 ASM, 1962, pp. 58–76.
- [6] S. Floreen, The physical metallurgy of maraging steels, *Metall. Rev.* 13 (1968) 115–128, <https://doi.org/10.1179/mtr.1968.13.1.115>
- [7] K. Rohrbach, M. Schmidt, Maraging steel, in *ASM Handbook, Metals Park Vol. 1 ASM International*, 1991, pp. 793–800.
- [8] M.N. Rao, Progress in understanding the metallurgy of 18% nickel maraging steel, *Int. J. Mater. Res* 97 (2006) 1594–1607, <https://doi.org/10.3139/146.101418>
- [9] T. Allam, K.G. Pradeep, P. Köhnen, A. Marshal, J.H. Schleifenbaum, C. Haase, Tailoring the nanostructure of laser powder bed fusion additively manufactured maraging steel, *Addit. Manuf.* 36 (2020) 101561, <https://doi.org/10.1016/j.addma.2020.101561>
- [10] E.I. Galindo-Nava, W.M. Rainforth, P.E.J. Rivera-Díaz-del-Castillo, Predicting microstructure and strength of maraging steels: Elemental optimization, *Acta Mater.* 117 (2016) 270–285, <https://doi.org/10.1016/j.actamat.2016.07.020>
- [11] J. Zhang, M. Wang, L. Niu, J. Liu, J. Wang, Y. Liu, Z. Shi, Effect of process parameters and heat treatment on the properties of stainless steel CX fabricated by selective

- laser melting, *J. Alloy. Compd.* 877 (2021) 160062, <https://doi.org/10.1016/j.jallcom.2021.160062>
- [12] Y. Tian, R. Palad, L. Jiang, T. Dorin, K. Chadha, C. Aranas, The effect of heat treatments on mechanical properties of M789 steel fabricated by laser powder bed fusion, *J. Alloy. Compd.* 885 (2021) 161033, <https://doi.org/10.1016/j.jallcom.2021.161033>
- [13] S. Ifergane, M. Pinkas, Z. Barkay, E. Brosh, V. Ezersky, O. Beeri, N. Eliaz, The relation between aging temperature, microstructure evolution and hardening of Custom 465[®] stainless steel, *Mater. Charact.* 127 (2017) 129–136, <https://doi.org/10.1016/j.matchar.2017.02.023>
- [14] C.Y. Chen, P.H. Chiu, Y.L. Yang, W.S. Liu, Z.W. Chen, Y.H. Lin, Y.C. Kang, Insight on nano-sized precipitate-hardened Ti-Mo 11Cr-11Ni martensitic stainless steel, *Mater., Today Commun.* 31 (2022) 103454, <https://doi.org/10.1016/j.mtcomm.2022.103454>
- [15] R. Schnitzer, M. Schober, S. Zinner, H. Leitner, Effect of Cu on the evolution of precipitation in an Fe–Cr–Ni–Al–Ti maraging steel, *Acta Mater.* 58 (2010) 3733–3741, <https://doi.org/10.1016/j.actamat.2010.03.010>
- [16] M.C. Niua, L.C. Yind, K. Yang, J.H. Luane, W. Wang, Z.B. Jiaoc, Synergistic alloying effects on nanoscale precipitation and mechanical properties of ultrahigh-strength steels strengthened by Ni₃Ti, Mo-enriched, and Cr-rich co-precipitates, *Acta Mater.* 209 (2021) 116788, <https://doi.org/10.1016/j.actamat.2021.116788>
- [17] M. Niu, G. Zhou, W. Wang, M.B. Shahzad, Y. Shan, K. Yang, Precipitate evolution and strengthening behavior during aging process in a 2.5 GPa grade maraging steel, *Acta Mater.* 179 (2019) 296–307, <https://doi.org/10.1016/j.actamat.2019.08.042>
- [18] S. Zeisl, A. Lassnig, A. Hohenwarter, F. Mendez-Martin, Precipitation behavior of a Co-free Fe–Ni–Cr–Mo–Ti–Al maraging steel after severe plastic deformation, *Mater. Sci. Eng. A* 833 (2022) 142416, <https://doi.org/10.1016/j.msea.2021.142416>
- [19] J. Tian, W. Wang, H. Li, M.B. Shahzad, Y. Shan, Z. Jiang, K. Yang, Effect of deformation on precipitation hardening behavior of a maraging steel in the aging process, *Mater. Charact.* 155 (2019) 109827, <https://doi.org/10.1016/j.matchar.2019.109827>
- [20] J.I. Suk, S.H. Hong, S.W. Nam, Crystallographic orientation relationships among η -Ni₃Ti precipitate, reverted austenite, and martensitic matrix in Fe-10Cr-10Ni-2W maraging alloy, *Metall. Mater. Trans. A* 24 (1993) 2643–2652, <https://doi.org/10.1007/BF02659488>
- [21] A. Shekhter, H.I. Aaronson, M.R. Miller, S.P. Ringer, E.V. Pereloma, Effect of aging and deformation on the microstructure and properties of Fe–Ni–Ti maraging steel, *Metall. Mater. Trans. A* 35 (2004) 973–983, <https://doi.org/10.1007/s11661-004-0024-9>
- [22] F. Zhu, Y.F. Yin, R.G. Faulkner, Microstructural control of maraging steel C300, *Mater. Sci. Technol.* 27 (2011) 395–405, <https://doi.org/10.1179/026708309x12506933873503>
- [23] V.K. Vasudevan, S.J. Kim, C.M. Wayman, Precipitation reactions and strengthening behavior in 18 Wt Pct nickel maraging steels (<https://doi.org/ezprox-y.bgu.ac.il/>), *Metall. Mater. Trans. A* 21 (1990) 2655–2668, <https://doi.org/10.1007/BF02646061>
- [24] C. Zhang, C. Wang, S.L. Zhang, Y.L. Ding, Q.L. Ge, J. Su, Effect of aging temperature on the precipitation behavior and mechanical properties of Fe–Cr–Ni maraging stainless steel, *Mater. Sci. Eng. A* 806 (2021) 140763, <https://doi.org/10.1016/j.msea.2021.140763>
- [25] C.Y. Chen, P.H. Chiu, W.S. Liu, Z.W. Chen, Y.H. Lin, Y.C. Kang, Interaction between η -Ni₃Ti and reversed austenite within Custom 465 stainless steel: experimental evidence and related patents investigation, *Mater. Sci. Eng. A* 839 (2022) 142852, <https://doi.org/10.1016/j.msea.2022.142852>
- [26] E.F. Rauch, M. Véron, Methods for orientation and phase identification of nano-sized embedded secondary phase particles by 4D scanning precession electron diffraction, *Acta Crystallogr. B Struct. Sci. Cryst. Eng. Mater.* 75 (2019) 505–511, <https://doi.org/10.1107/S2052520619007583>
- [27] M. Shmulevitch, R.Z. Shneck, An approach to calculate the elastic interaction energy of inhomogeneous precipitates: application to γ' -Ni₃Ti in A-286 steel, *J. Appl. Mech.* 85 (2018) 8, <https://doi.org/10.1115/1.4040117>
- [28] M. Degeiter, Y. Le Bouar, B. Appolaire, M. Perrut, A. Finel, Instabilities in the periodic arrangement of elastically interacting precipitates in nickel-base superalloys, *Acta Mater.* 187 (2020) 41–50, <https://doi.org/10.1016/j.actamat.2020.01.022>
- [29] G. Esteban-Manzanares, R. Alizadeh, I. Papadimitriou, D. Dickel, C.D. Barrett, J. Llorca, Atomistic simulations of the interaction of basal dislocations with MgZn₂ precipitates in Mg alloys, *Mater. Sci. Eng. A* 788 (2020) 139555, <https://doi.org/10.1016/j.msea.2020.139555>
- [30] F. Siska, L. Stratil, J. Cizek, T. Guo, M. Barnett, Numerical analysis of twin-precipitate interactions in magnesium alloys, *Acta Mater.* 202 (2021) 80–87, <https://doi.org/10.1016/j.actamat.2020.10.053>
- [31] I. Adlakha, P. Garg, K.N. Solanki, Revealing the atomistic nature of dislocation-precipitate interactions in Al–Cu alloys, *J. Alloy. Compd.* 797 (2019) 325–333, <https://doi.org/10.1016/j.jallcom.2019.05.110>
- [32] C. Liu, P. Shanthraj, J.D. Robson, M. Diehl, S. Dong, J. Dong, D. Raabe, On the interaction of precipitates and tensile twins in magnesium alloys, *Acta Mater.* 178 (2019) 146–162, <https://doi.org/10.1016/j.actamat.2019.07.046>
- [33] Y. Hu, W.A. Curtin, Modeling peak-aged precipitate strengthening in Al–Mg–Si alloys, *J. Mech. Phys. Solids* 151 (2021) 104378, <https://doi.org/10.1016/j.jmps.2021.104378>
- [34] M. Doi, T. Miyazaki, T. Wakatsuki, The effects of elastic interaction energy on the γ' precipitate morphology of continuously cooled nickel-base alloys, *Mater. Sci. Eng.* 74 (1985) 139–145, [https://doi.org/10.1016/0025-5416\(85\)90427-6](https://doi.org/10.1016/0025-5416(85)90427-6)
- [35] M. Cottura, Y. Le Bouar, B. Appolaire, A. Finel, Rôle of elastic inhomogeneity in the development of cuboidal microstructures in Ni-based superalloys, *Acta Mater.* 94 (2015) 15–26, <https://doi.org/10.1016/j.actamat.2015.04.034>
- [36] L. Liu, Z. Chen, Y. Wang, Elastic strain energy induced split during precipitation in alloys, *J. Alloy. Compd.* 661 (2016) 349–356, <https://doi.org/10.1016/j.jallcom.2015.11.201>
- [37] Y. Xingfu, T. Sugui, D. Hongqiang, Y. Huichen, W. Minggang, S. Lijuan, C. Shusen, Microstructure evolution of a pre-compression nickel-base single crystal superalloy during tensile creep, *Mater. Sci. Eng. A* 506 (2009) 80–86, <https://doi.org/10.1016/j.msea.2008.12.006>
- [38] J. Chen, C. Liu, Q. Li, H. Zhao, A three-dimensional characterization method for the preferentially oriented precipitation of Ω -phase in stress-aged Al–Cu–Mg–Ag single crystal, *Mater. Charact.* 153 (2019) 184–189, <https://doi.org/10.1016/j.matchar.2019.04.035>
- [39] L. Zhong, C. Chen, Y. Wang, Y. Dou, Directional-dependent precipitate microstructure and mechanical properties of tensile and compressive stress-assisted aged Mg–Zn alloys, *J. Alloy. Compd.* 164728 (2022), <https://doi.org/10.1016/j.jallcom.2022.164728>
- [40] E.L. Solomon, A.R. Natarajan, A.M. Roy, V. Sundararaghavan, A. van der Ven, E.A. Marquis, Stability and strain-driven evolution of β' precipitate in Mg–Y alloys, *Acta Mater.* 166 (2019) 148–157, <https://doi.org/10.1016/j.actamat.2018.12.026>
- [41] H. Mao, Y. Kong, D. Cai, M. Yang, Y. Peng, Y. Zeng, Y. Du, β'' needle-shape precipitate formation in Al–Mg–Si alloy: Phase field simulation and experimental verification, *Comput. Mater. Sci.* 184 (2020) 109878, <https://doi.org/10.1016/j.commatsci.2020.109878>
- [42] G. Boussinot, A. Finel, Y. Le Bouar, Phase-field modeling of bimodal microstructures in nickel-based superalloys, *Acta Mater.* 57 (2009) 921–931, <https://doi.org/10.1016/j.actamat.2008.10.039>
- [43] J.Z. Zhu, T. Wang, A.J. Ardell, S.H. Zhou, Z.K. Liu, L.Q. Chen, Three-dimensional phase-field simulations of coarsening kinetics of γ' particles in binary Ni–Al alloys, *Acta Mater.* 52 (2004) 2837–2845, <https://doi.org/10.1016/j.actamat.2004.02.032>
- [44] H. Zapolsky, S. Ferry, X. Sauvage, D. Blavette, L.Q. Chen, Kinetics of cubic-to-tetragonal transformation in Ni–V–X alloys, *Philos. Mag.* 90 (2010) 337–355, <https://doi.org/10.1080/14786430903179562>
- [45] A. Suzukia, H. Kojimab, T. Matsuo, M. Takeyama, Alloying effect on stability of multi-variant structure of Ni₃V at elevated temperatures, *Intermetallics* 12 (2004) 969–975, <https://doi.org/10.1016/j.intermet.2004.02.028>
- [46] Y. Ni, Y.M. Jin, A.G. Khachatryan, The transformation sequences in the cubic to tetragonal decomposition, *Acta Mater.* 55 (2007) 4903–4914, <https://doi.org/10.1016/j.actamat.2007.05.016>
- [47] A. Artemev, Y. Jin, A.G. Khachatryan, Three dimensional phase field model of proper martensitic transformation, *Acta Mater.* 49 (2001) 1165–1177, [https://doi.org/10.1016/S1359-6454\(01\)00021-0](https://doi.org/10.1016/S1359-6454(01)00021-0)
- [48] W.A. Soffa, D.E. Laughlin, N. Singh, Interplay of ordering and spinodal decomposition in the formation of ordered precipitates in binary fcc alloys: Role of second nearest-neighbor interactions, *Philos. Mag.* 90 (2010) 287–304, <https://doi.org/10.1080/14786430903127520>
- [49] S. Ifergane, R. Ben David, E. Sabatani, B. Carmeli, O. Beeri, N. Eliaz, Hydrogen diffusivity and trapping in custom 465 stainless steel, *J. Electrochem. Soc.* 165 (3) (2018) C107–C115, <https://doi.org/10.1149/2.0261803jes>
- [50] S. Ifergane, E. Sabanati, B. Carmeli, Z. Barkay, V. Ezerski, O. Beeri, N. Eliaz, Hydrogen diffusivity measurements and microstructural characterization of Custom 465 stainless steel, *Electrochim. Acta* 178 (2015) 494–503, <https://doi.org/10.1016/j.electacta.2015.08.016>
- [51] X. Li, Z. Yin, A computer-simulated electron diffraction analysis of precipitates in 18 Ni (350) maraging steel, *Mater. Lett.* 23 (1995) 269–272, [https://doi.org/10.1016/0167-577X\(95\)00053-4](https://doi.org/10.1016/0167-577X(95)00053-4)
- [52] M. Shmulevitch, L. Meshi, M. Pinkas, R.Z. Shneck, Elastic consideration of the precipitation in model alloys of maraging steels: theory and experimental validation, *J. Mater. Sci.* 50 (2015) 4970–4979, <https://doi.org/10.1007/s10853-015-9044-7>
- [53] U. Dahmen, Orientation relationships in precipitation systems, *Acta Met.* 30 (1) (1982) 63–73, [https://doi.org/10.1016/0001-6160\(82\)90045-1](https://doi.org/10.1016/0001-6160(82)90045-1)
- [54] T. Mura, *Micromechanics of Defects in Solids*, The Hague, Martinus Nijhoff Publishers, The Netherlands, 1987.
- [55] A.G. Khachatryan, *Theory of Structural Transformations in Solids*, Wiley, New York, 1983.
- [56] J.D. Eshelby, Elastic inclusions and inhomogeneities. In: N.I. Sneddon, R. Hill (eds): *Progress in Solid Mechanics*, Vol. 2. Amsterdam, North Holland, 1961, p. 89.
- [57] H.L. Zhang, N. Al-Zoubi, B. Johansson, L. Vitos, Alloying effects on the elastic parameters of ferromagnetic and paramagnetic Fe from first-principles theory, *J. Appl. Phys.* 110 (2011) 07307, <https://doi.org/10.1063/1.3644907>
- [58] B.I. Choi, Y.Y. Earmme, Interactions of spherical precipitates in an anisotropic matrix, *Mech. Mater.* 5 (1986) 121–136, [https://doi.org/10.1016/0167-6636\(86\)90028-1](https://doi.org/10.1016/0167-6636(86)90028-1)
- [59] W.C. Johnson, J.O. Lee *Elastic Fields, of Inhomogeneous Precipitate in Phase Transformation*, Elsevier, Amsterdam, 1986, pp. 115–139.
- [60] V.K. Vasudevan, S.J. Kim, C.M. Wayman, Precipitation reactions and strengthening behavior in 18 Wt Pct nickel maraging steels, *Metall. Trans. A* 21 (1990) 2655–2668, <https://doi.org/10.1007/BF02646061>